Bulletin of Earthquake Engineering (2025) 23:5161–5190
https://doi.org/10.1007/s10518-025-02192-z

ORIGINAL ARTICLE

Use of post-earthquake point cloud data for forensic evaluation of failures in masonry structures

Yilong Yang[1] · Elif Durgut[2] · Medine Ispir[2] · Bora Pulatsu[3] · Sinan Acikgoz[1]

Received: 10 December 2024 / Accepted: 24 May 2025 / Published online: 25 June 2025

Abstract

Post-earthquake reconnaissance of engineering structures aims to collect the essential data required for forensic investigations of failures. These investigations inform time-critical repair, stabilisation and demolition decisions after an earthquake. Current reconnaissance procedures rely on visual observations and manual surveying, which do not provide adequate data for the forensic analysis of historic masonry structures. This study shows how an alternative form of data, point clouds from laser scanning and photogrammetry, can be used to conduct detailed forensic work. Case studies from the 2023 Turkey earthquakes are used to illustrate how point clouds were employed to 1) quantify the geometry of load-bearing systems, 2) assess construction quality, 3) detect geometric distortions and defects, and 4) provide data to generate and evaluate numerical models. The examples highlight the new insight provided by this alternative form of data. The dataset collected as a part of this study is shared open access to enable further investigations: https://github.com/Yilong-Yang/Shared-Data---BEE-2025.

keywords Reconnaissance · Earthquakes · Masonry · Point clouds · Damage assessment

✉ Yilong Yang
dgianyang@gmail.com

Elif Durgut
durgut17@itu.edu.tr

Medine Ispir
ispirm@itu.edu.tr

Bora Pulatsu
borapulatsu@cunet.carleton.ca

Sinan Acikgoz
sinan.acikgoz@eng.ox.ac.uk

[1] University of Oxford, Oxford, UK

[2] Istanbul Technical University, Istanbul, Turkey

[3] Carleton University, Ottawa, Canada

1 Introduction

Post-earthquake reconnaissance data plays a key role in disaster management. Traditionally, data was collected during field missions with form-filling, note-taking, manual surveying and photography (Contreras et al. 2021). More recently, hybrid data collection strategies have been adopted by field teams to benefit from recent advancements in remote sensing and data science technologies. For example, by using high resolution satellite images, instances of building collapse in the earthquake zone can be identified and localised ahead of a field mission (Saito et al. 2004; Tong et al. 2012; Aktaş et al. 2024). This data can be augmented by witness reports from publicly available sources such as news sites and social media platforms (Aktaş et al. 2024, 2022).

Field missions are necessary to obtain key engineering data which may not be available from remote sources. For forensic failure evaluations, it is necessary to collect key geometric information, such as the dimensions of structural components (Hariri-Ardebili and Sattar 2024). Detailed measurements of structural damage (e.g. geometric distortions and cracks) are also needed. This data is traditionally collected using manual surveying (tape measures, crack rulers, measuring wheels and levelling devices) (McCormac et al. 2012; Bianchi et al. 2024) and photography (Whitworth et al. 2022).

Post earthquake data collection with traditional techniques is fraught with difficulties, especially for historic masonry structures. In these structures, the load-bearing components may be non-rectangular and dimensions may vary significantly in size from one component to another. Furthermore, drawings may not be available. Under these conditions, documenting the geometry comprehensively with manual surveying techniques may be infeasible due to the excessive time requirements. Furthermore, traditional approaches for recording damage require direct physical access to the areas with geometric distortions and cracks, which can be unsafe.

Ideally, post-earthquake data collection from historic masonry structures should comprehensively address the following four aspects:

1. characterise structural geometry
2. assess construction quality
3. quantify geometric distortions and defects
4. provide data to generate and evaluate numerical models

Data collection should be rapid and safe. Although there have been limited earthquake engineering applications to date, scientific papers from cognate fields suggest that laser scanning and photogrammetry may provide the means to collect the required data. The literature review below discusses why the four aspects listed above need to be addressed and how point cloud data may be used for this purpose.

Regarding the first aspect, it is evident that quantitative information on structural geometry is needed to evaluate the load-carrying capacity of structures. Bozyigit et al. (2024); Lourenço et al. (2013); Lourenco and Roque (2006) used simplified geometric indices (such as the ratio of the area of earthquake-resistant walls to the total floor area) to assess the safety of structures subjected to lateral loads. In the absence of structural drawings, Bozyigit et al. (2024) used point cloud data to calculate the indices. Point clouds have also been used

to generate numerical models to calculate the load capacity of structures (Milani et al. 2013; Conde et al. 2017).

Poorly constructed masonry structural components may not be able to resist seismic loads monolithically and may disaggregate. Borri et al. (2020) explains how disaggregation is inversely correlated with construction quality. To define quality, they use Masonry Quality Index (MQI) (Borri et al. 2015)- an index that can be calculated from the geometric and visual evaluation of unit/mortar sizes and arrangements. Collecting post-earthquake data capable of supporting the calculation of MQI (i.e. Aspect 2) can thus help forensic evaluations related to disaggregation. More broadly, the MQI data can also be used as a guide to generate representative numerical models of the structure, where key aspects of masonry stereotomy are explicitly represented (Truong-Hong and Laefer 2013; Barazzetti et al. 2015; Szabó et al. 2024). Although most previous studies (e.g. Bozyigit et al. (2024); Borri et al (2020; 2015)) calculate MQI qualitatively, recent success with masonry point cloud unit segmentation (Valero et al. 2018) suggests the feasibility of quantitative MQI calculations.

In Sacco et al. (2024); Ye et al. (2018); Pesci et al. (2013), point clouds of deformed surfaces are compared against primitive shapes (e.g. idealised geometries approximating the undeformed geometry) to evaluate distortions of structures over time. Other studies highlight how point clouds can be used to detect and measure cracks. There are notable geometric limitations associated with crack detection (Laefer et al. 2014); in most cases, detection is only possible for centimetre-scale cracks when multiple measurement points directly align with the crack's location. By using the distinct geometric or radiometric information (relating to the intensity of the laser beams in terrestrial laser scans or colour in photogrammetry point clouds) of crack points, the crack edges can be identified (Stałowska et al. 2022). Measurement of crack widths can then be conducted by measuring distances between opposite crack edges. In relation to this, previous studies also explored the limitations of various algorithms to measure distances between point clouds. For instance, Lague et al. (2013) highlights that the distances between individual points provide noisy estimates of the distance and recommends local plane fitting before conducting the measurements.

Findings from the reviewed studies suggest that post-earthquake point clouds can be used to conduct distortion and crack measurements (albeit with some limitations), addressing Aspect 3. Aspect 4 then involves using all of the aforementioned point cloud data processing techniques to generate and evaluate numerical models (e.g. Sacco et al. (2023); Napolitano et al. (2019)). Automated generation of numerical models from point clouds (Kassotakis et al. 2020; Castellazzi et al. 2022) has been explored within this context but further research is needed for real-world applications of this technique, which remains outside the scope of this study.

The current paper synthesises previous techniques and develops new data analysis procedures to use point clouds for the post-earthquake forensic evaluation of masonry structures. The techniques are applied to several structures damaged during the 2023 Turkey earthquake sequence. Section 2 details the measurement technologies, data collection and pre-processing procedures associated with point cloud data. Section 3 illustrates the characterisation of building geometries and construction quality. Section 4 presents distortion evaluation and crack measurements. Section 5 discusses a case study which involves the numerical simulation of a church, guided by point cloud data. Section 6 concludes the paper with a brief summary of findings.

2 Technology, data collection and pre-processing

2.1 Background: Terrestrial Laser Scanning (TLS) and photogrammetry

TLS detects objects through its ranging system, where the emitted laser beam with the given azimuthal (α) and elevation (β) angles are reflected from the target surface, as shown in Fig. 1. From the reflected beams, the distance (S) between the scanner and the reflection point is measured. The world coordinates of each detected point (X_p, Y_p, Z_p) can then be calculated:

$$\begin{cases} X_p = S\cos\beta\cos\alpha \\ Y_p = S\cos\beta\sin\alpha \\ Z_p = S\cos\beta \end{cases} \tag{1}$$

Alternatively, photogrammetry can be used to produce 3D coordinates of objects by analysing 2D images captured from various locations and perspectives. This process relies on the collinearity of key points (see Fig. 1). The process of determining (X_p, Y_p, Z_p), the world coordinates of the detected key point, using the common image points (x_{p1}, y_{p1}) and (x_{p2}, y_{p2}), is detailed in Awange and Kiema (2019).

Compared to traditional manual surveying, the advantages of TLS and photogrammetry can be summarised as follows:

- Non-contact: The scanning and photography processes do not require unsafe access.
- Fast and massive sampling capability: Both technologies enable fast and high-density data collection.
- Position, radiometry and colour information: Apart from 3D positional information, the obtained data features reflected laser intensity values and/or RGB colour information.
- Easy acquisition: Data collection is highly automated.

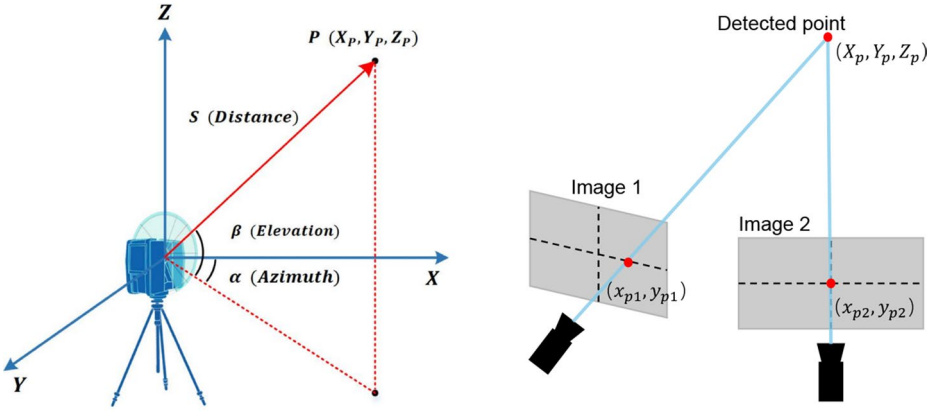

(a) TLS, image from Wu et al (2022). (b) Photogrammetry.

Fig. 1 Schematics of TLS and photogrammetry, demonstrating how the world coordinates of a detected point are determined

TLS and photogrammetry technologies both produce complementary point cloud data. TLS devices can collect more than 1M points per second. Due to their superior speed, they are well suited to capturing large geometric volumes quickly. On the other hand, TLS data struggles to reproduce colour information accurately due to the resolution mismatch between point clouds and the internal scanner cameras. Parts of structures which are occluded from the ground (e.g. roof surfaces) cannot be captured by TLS. Conversely, colour captured by cameras is an essential part of geometry reconstruction and is likely to be more accurate than TLS. Furthermore, aerial images can be readily captured with a drone, covering the missing parts from TLS.

2.2 Data collection and pre-processing

2.2.1 Investigated structures

The point cloud data used in this paper was collected during two field missions following the 2023 Turkey earthquake sequence: the first between 13–17 March 2023 and the second between 11–19 April 2023. During the missions, 29 historic stone masonry structures were examined. The building IDs, names, locations, and point cloud data collection modalities (e.g. laser scanning, terrestrial or aerial photography, see Fig. 2) are provided in the appendix (see Table A1). Data from only some of these structures are examined in this paper. In the following sections, the 19th century St Ilias Church from Samandag district of Hatay province (identified as building C7 in Table A1) will be used to exemplify data collection and pre-processing.

(a) TLS. (b) Aerial photography.

Fig. 2 Photographs showing different modalities of data acquisition

2.2.2 Terrestrial laser scanning

Laser scanning was performed with two different scanners-Faro Focus S70 and M70. On average, each scan required 2 minutes for completion and the resulting point cloud contained 44 million points with a point spacing of 6 mm at 10 m ranging distance. The manufacturer specifies the accuracy of each point as 2 to 3 mm at a ranging distance of 25 m. Colour was occasionally acquired but was not used in the analyses. The internal GPS, compass, and inclinometer measurements were used for improved registration.

For each surveyed structure, multiple scans were taken at different locations of the interior and exterior. For instance, 10 scans were collected for St. Ilias Church. To generate the final point cloud of the structure, registration of separate scans was performed using the FARO SCENE software, using cloud to cloud registration whenever possible. Manual tie point/plane registration was used in case of limited overlap. The final registered point cloud of St Ilias is shown in Fig. 3, where the tiled roof surface is missing due to the terrestrial placement of the scanners.

2.2.3 Photogrammetry

Complementary point clouds of the surveyed structures were generated from terrestrial and aerial photography with a Canon EoS 6D Mark II camera and a Mavic 2 Pro drone respectively. A point cloud of the exterior south façade of St Ilias was generated from 63 photographs using the Agisoft Metashape Professional software (see Fig. 3). This point cloud

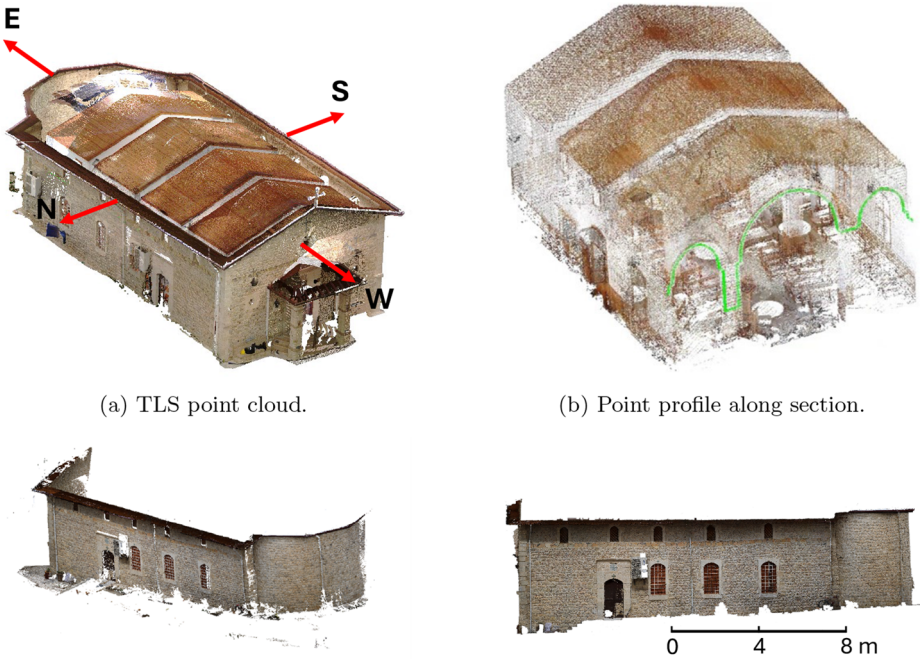

(a) TLS point cloud.

(b) Point profile along section.

(c) Photogrammetry point cloud of the south wall.

(d) Orthophoto of the south wall.

Fig. 3 Point clouds and orthophotographs of St Ilias church obtained from TLS and photogrammetry

exhibits a higher point density than the terrestrial laser scans (average spacing of 4.65 mm versus 20.0 mm in the investigated area).

2.2.4 Pre-processing

Point clouds generated from laser scanning and photogrammetry can be pre-processed to generate informative data of other forms, including point profiles and orthophotos. Point profiles are polylines defined over a specified section across a structure. An example is shown in Fig. 3 where the green points represent the point profile along the arched frame cross-section of St Ilias. Orthophotos are images that have been geometrically corrected to eliminate camera and perspective distortions (see Fig. 3). They enable direct measurement and analysis of critical planar dimensions.

3 Point cloud post-processing for forensic evaluation

3.1 Geometry characterisation

Basic geometry information derived from 3D models can be useful to conduct preliminary forensic assessments. This aspect is demonstrated using the post-earthquake point cloud data of St Ilias church.

The floor plan of St Ilias (Fig. 4) was obtained by extracting point profiles from a horizontal plane close to ground level. The variable thickness of the longitudinal and transverse walls is evident in this figure.

The wall-to-floor area ratios (Lourenco and Roque 2006) are calculated as 15.1% in the longitudinal direction and 8.1% in the transverse direction. Notably, deriving these areas from point clouds is straightforward, whereas manual surveying would have required signifi-

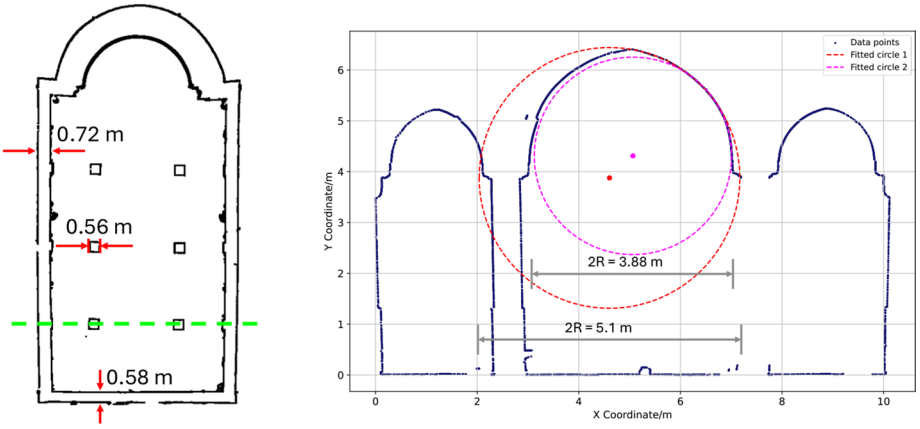

(a) Point profile along floor plan.

(b) Point profile along the arches.

Fig. 4 (a) Floor plan dimension measurements and (b) primitive shape fitting on arch structures using St Ilyas Church TLS point clouds. The green dashed line in (a) indicates the location of the point profile in (b)

cant effort. In the longitudinal direction, the ratio exceeds the recommended safety threshold of 10% (Meli 1998) (applicable for peak ground accelerations up to 0.25 g, approximately matching the observed PGA for St. Ilias). However, the transverse direction falls short of this threshold. It is important to note that this apparent deficiency in the transverse direction does not consider the contribution of the arched frames within the structure, which also resisted the loads. To investigate this further, geometry of this load-carrying element needs to be characterised. In the absence of structural drawings, either manual surveys or point clouds can be used to characterised geometry. However, the non-circular arch geometry renders manual surveying impractical.

The geometric analysis of the arched frame in St Ilias is conducted with a transverse point profile (indicated by the green lines in Figs. 4a and 3b). Visualisation of the point profile is provided in Fig. 4b, where the central arch exhibits a width of 3.97 m and a height of 2.28 m. Reconstruction of the original geometry of the centre arch is done by iteratively fitting circles. Based on the minimisation of fitting errors, the geometry is identified as a four-centred arch whose geometric specifications are given in Fig. 4b. It should be noted that, since there exists a slip in the left half of the arch, only points belong to the right half are used for fitting.

These results exemplify how post-earthquake point cloud data may be used to obtain a wide variety of useful geometric characteristics. Point clouds enable an evaluation of geometric variability and facilitate rigorous characterisation of complex geometric components, which would be otherwise difficult and time-consuming with manual surveying.

3.2 Construction quality characterisation

Construction quality plays a key role in how a building responds to seismic loads. To analyse construction quality systematically Borri et al. (2015) defined a masonry quality index (MQI) using the following parameters: conservation state (SM), stone/brick dimensions (SD) and shapes (SS), wall leaf connections (WC), horizontality of bed joints (HJ), stagger properties of vertical joints (VJ), and mortar properties (MM). MQI is calculated evaluated as follows:

$$MQI = SM(SD + SS + WC + HJ + VJ + MM) \tag{2}$$

Based on the obtained numerical value for MQI, the analysed structure can be categorised into: A-good quality, B-average quality, and C-inadequate quality. This calculation can be done for different loading scenarios, namely, vertical, out-of-plane, and in-plane loads. Numerical values of quality parameters are evaluated based on either quantitative (e.g. see Table 1) or qualitative (e.g. see Table 2) criteria to determine compliance with fulfilment criteria. Three categories are defined - Not Fulfilled (NF), Partially Fulfilled (PF), and Fufilled (F). These categories are assigned specific numerical values (specific to each MQI parameter) to calculate the overall MQI.

The correspondence between MQI and structural disaggregation was observed by Bozyigit et al. (2024) where the structures damaged in the Turkey-Syria earthquakes 2023 were studied. However, the assessment of MQI in that study is largely based on the qualitative criteria, which can introduce bias. In this study, we present a semi-automated methodology for deriving quality parameters within the MQI framework from point cloud data. This

Table 1 Fulfilment criteria for MQI stone/brick dimension (SD) parameter. Table reproduced from Borri et al. (2015)

Category	Description
NF	Presence of more than 50% of elements with large dimension 0.7 $<$ 20cm
PF	Presence of more than 50% of elements with large dimension 20-40cm
F	Presence of more than 50% of elements with large dimension $>$ 40cm

Table 2 Fulfilment criteria for stone/brick shape (SS). Table reproduced from Borri et al. (2015)

Category	Description
NF	Rubble, rounded or pebble stonework (predominant) on both masonry leaves.
PF	Co-presence of rubble, rounded or pebble stonework and barely/perfectly cut stone and bricks on both masonry leaves;
	One masonry leaf made of perfectly cut stones or bricks;
	Masonry made of irregular (rubble, rounded, pebble) stones, but with presence of pinning stones
F	Barely cut stones or perfectly cut stones on both masonry leaves (predominant); Brickwork

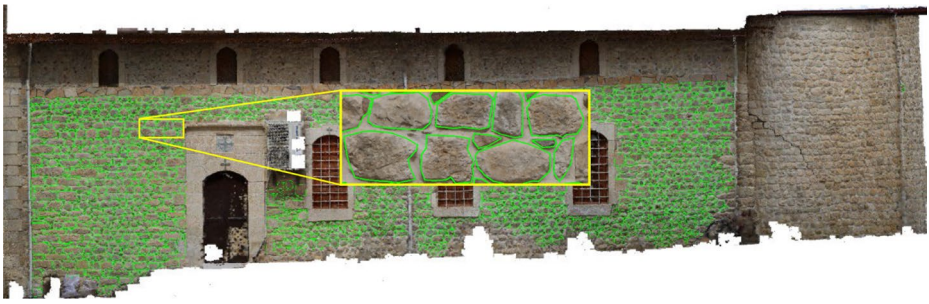

Fig. 5 Orthophoto of the south wall of St Ilyas church, obtained by pre-processing photogrammetry point clouds. The inset figure shows the manual segmentation of stone units with polylines

approach contrasts with conventional practices, which rely on manual interpretation and are inherently subjective, by providing a quantitative and objective means of assessment. To this end, new quantitative criteria are developed.

To demonstrate the procedure, an orthophotograph of the south wall of St. Ilias (see Fig. 5) is analysed. First, segmentation is performed by labelling each stone with its smallest enclosing polygon. Manual labelling was adopted since available image segmentation algorithms (such as the Watershed or the 2D wavelet transform (Valero et al. 2018) algorithms) did not demonstrate sufficient performance in this dataset, likely due to the similar colours of stones and mortar and insufficient density of point clouds. However, promising segmentation results (Loverdos and Sarhosis 2022; Ergün Hatir and İsmail İnce 2021; Ibrahim et al. 2019) obtained from neural networks suggest that automatic segmentation may be generalised in the future with deep learning algorithms. This can be integrated directly with the fully automated morphological analysis that will be developed next.

The two parameters concerned with units-SD and SS-are discussed first. In this work, we define the length of the major axis of the best fitted ellipse as the large dimension of each investigated stone. Given the threshold values in Table 1 for SD, the cumulative distribution function (CDF) of the large stone dimension is shown in Fig. 6a where two examples of the fitted ellipses are also provided inset. It can be seen that stone dimensions fall into the PF category with roughly 60% of the larger dimension of stones greater than 20 cm.

In the original criteria of SS (Table 2), no quantitative descriptions are given. To this end, a new measure called the Rectangularity Index, RI, is employed to quantitatively measure SS. It is defined as follows:

$$RI = \frac{A}{A_{Bbox}} \tag{3}$$

where A is the area of the stone/brick and A_{Bbox} is the area of the smallest bounding box of each stone. RI ranges from 0 to 1. The nearer RI approaches 1, the more the shape resembles a rectangle and vice versa. In this study, orthophotos were generated using a plane fitted to the wall surface. The stones were arranged using horizontal courses, which were represented with horizontal lines in the image, indicating minimal skew. If the stones in the orthophoto are not aligned to the horizontal image axis due to a non–zero skew angle, Principal Component Analysis can be adopted to determine the skew angle and rotate the image before applying Equation 3 to calculate rectangularity." With RI, the criteria of SS is reformulated as shown in Table 3. The CDF of SS using the reformulated criteria is shown in Fig. 6b, where two sample stones at the threshold values are shown inset. SS of the structure is identified as PF, with approximately 80% of the stones having RI greater than 0.7.

The thickness of mortar can serve as a reference length for other calculations. This parameter is determined by calculating the average shortest distance between each stone and its eight nearest neighbours. The neighbours of each target stone are identified as the closest stones located in eight distinct radial directions, as shown in Fig. 7. Properties of verticality of head joints (VJ) and horizontality of bed joints (HJ) are used to assess the shear capacity and degree of interlocking of masonry. The VJ criteria relies on the definition of the minimal length ratio, M_{I}, which is a non-dimensional value defined as the ratio between the mini-

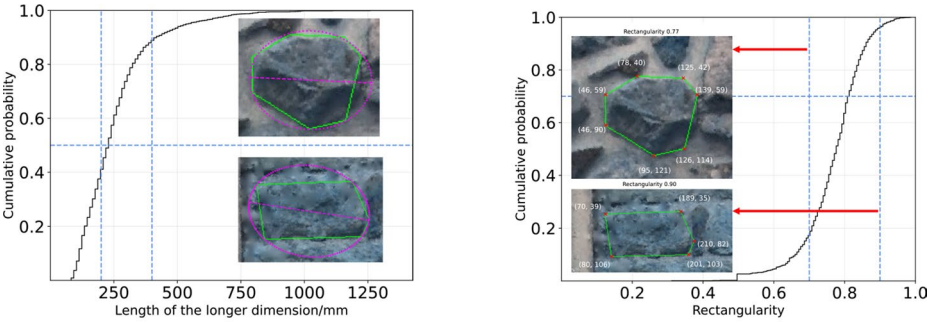

(a) Stone dimension (SD). (b) Stone shape (SS).

Fig. 6 Quantitative evaluation of MQI parameters of (a) SD and (b) SS using cumulative density function distributions of the largest dimensions and the rectangularity index of investigated stones of the south wall of St Ilyas church

Table 3 Reformulated fulfillment criteria for stone/brick dimension parameter (SD)

Category	Description
NF	Presence of more than 75% of elements with 0.7 > RI
PF	Presence of more than 75% of elements with 0.7 < RI < 0.9
F	Presence of more than 75% of elements with 0.9 < RI

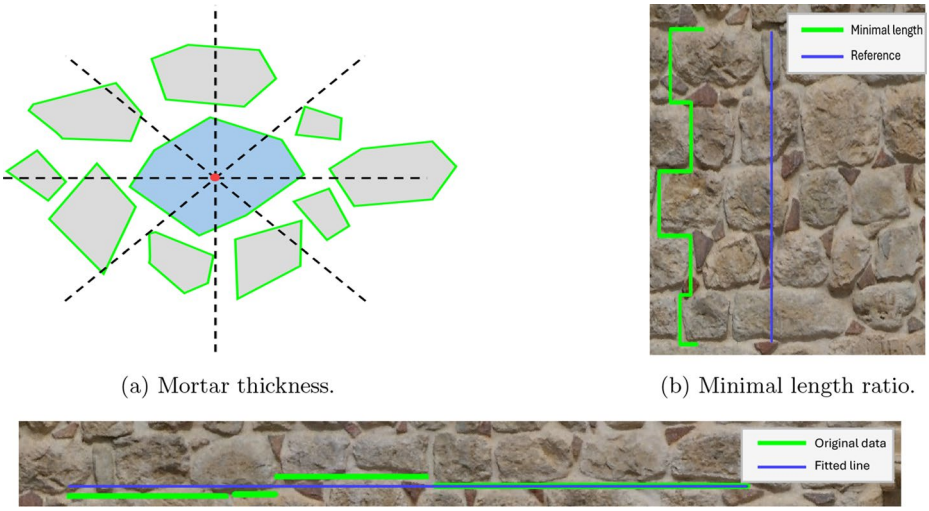

(a) Mortar thickness. (b) Minimal length ratio.

(c) Relative deviation.

Fig. 7 Schematics and photographs illustrating the techniques used for measuring (a) mortar thickness, (b) minimal length ratio and (c) relative deviation. These geometric parameters are used in the calculation of the MQI parameters HJ and VJ

mum distance connecting two points on the wall surface passing only through mortar joints (L_{min}) and the straight distance between the two points ($L_{reference}$) (Borri et al. 2015):

$$M_l = \frac{L_{min}}{L_{reference}} \tag{4}$$

The straight distance is usually evaluated over a distance of 1 m, but smaller values down to 50 cm can be used. An example of how M_l is evaluated is illustrated in Fig. 7b.

The HJ criteria was originally defined in a qualitative manner, to support the estimation of the lateral and compression strengths of walls. To facilitate an objective definition of this parameter, numerical values of HJ are evaluated by finding the relative deviation from the best fitted horizontal line, as demonstrated in Fig. 7a. An equation to evaluate the relative deviation is given as:

$$\delta_{rel} = \frac{\sum_{i=1}^{N} d(l^i_{seg}, l_{fit})|l^i_{seg}|}{t\sum_{i=1}^{N}|l^i_{seg}|} \tag{5}$$

Table 4 Statistical evaluation of the geometric parameters (a) mortar thickness, (b) minimal length ratio and (c) relative deviation calculated for the south wall of St Ilias church

Parameter	Mean	Standard deviation	Sample size
Mortar thickness (mm)	50.80	19.70	1790
Minimal length ratio, M_l	1.716	0.151	12
Relative deviation (mm)	43.20%	12.33%	6

Table 5 Reformulated fulfillment criteria for the MQI parameter-horizontality of bed joints (HJ) in terms of relative deviation, δ_{rel}

Category	Description
NF	150% $>\delta_{rel}$
PF	50% $>\delta_{rel}>$ 150%
F	50% $<\delta_{rel}$

where N is the total number of line segments, l^i_{seg} is the ith line segment, l_{fit} is the fitted line segment, $d(\cdot,\cdot)$ is the function evaluating the perpendicular distance between 2 line segments, $|\cdot|$ is the norm/length operator, and t is the average mortar thickness. The fulfilment criteria shown in Table 5 are proposed for the calculations.

The aforementioned parameters are measured at randomly selected locations across the south wall of St Ilias Church. The final statistics are summarised in Table 4. It can be noted that VJ and HJ are both fulfilled. From these parameters, the MQI of the south wall of St. Ilias Church is calculated as 4.55, assuming PF for quality parameters which cannot be assessed via geometric data alone (e.g. WC, MM and SM). This wall is identified as average construction quality based on the original classification proposed by Borri et al. (2015). Since only the structures which are classified as Class C (poor quality) are expected to experience disaggregation during the earthquakes, this classification for St Ilias can be considered consistent with the observations. It should be clarified that the MQIs of different walls may be different. In Bozyigit et al. (2024), the MQIs of the more recently constructed chancel arch spandrels were examined. These were classified as Class C upon a qualitative evaluation, which was in accordance with the disaggregation failures observed.

This section developed new analysis procedures and criteria for MQI-based construction quality evaluation from point clouds. The procedure developed here can also be a useful tool for automated pre-screening of construction quality in masonry buildings from point clouds (Cardani and Binda 2015) or to guide the MQI-based automated generation of numerical models which faithfully represent stereotomy observed in the data (Szabó et al. 2024).

4 Damage measurement

4.1 Geometric distortions

4.1.1 St. Ilias Church

As mentioned in Section 3, the arched frames of St Ilias contributed to the load-resistance of the building in the transverse direction. During this action, geometric distortions occurred due to relative movements between the voussoirs. Quantifying this damage is challenging using manual surveying techniques, as the affected locations are not easily accessible. With

the non-contact TLS point cloud data, the voussoir displacements are estimated straightforwardly by finding the closest distances between the point profile (Fig. 4) and the assumed original geometry, as identified earlier in Fig. 4 from the right side of the arch. In Fig. 8, the right half of the arch demonstrates negligible differences from the reference geometry, as expected. Meanwhile, the left half exhibits clear deviations and sharp discontinuities due to sliding between voussoirs. The maximum deviation is 6.0 cm, aligning with point measurements of relative displacements between voussoirs, which indicate ~6.3 cm of sliding at the same location (refer to the inset in Fig. 8). This deviation is based on an assumed geometry; its formation is attributed to the earthquake since pre-earthquake photographs do not indicate the presence of such distortion in the arches. Within this context, it is worth emphasising that deviations identified using this method cannot be attributed to earthquakes without additional evidence.

4.1.2 Residential building at Vakifli

TLS point cloud data collected from a two-storey residential building in Vakifli Village of Samandag District of Hatay province are examined herein (Fig. 9a). This building is referred to as Vakifli #2 building, following the naming convention in Sürmeli (2019) and it is represented with ID R5 in Table A1.

Point clouds of this building are examined since it exhibited counter-intuitive failure modes. Out of plane failures were observed in the transverse E and W walls of this building, despite good corner detailing. This failure appears to have been facilitated by a lack of diaphragm behaviour; photographs (e.g. Figure 9a) indicate that the timber floor structures are one-way spanning and did not restrain the out of plane movements in the E–W direction. Furthermore, an unusual bulging behaviour was visually observed on the northern wall of the building (Figure 9b). While it would be challenging to use manual surveying techniques to quantify this distortion, examination of bulging could be carried out simply by comparing the post-earthquake point cloud to a primitive geometry (e.g. a vertical plane in this case),

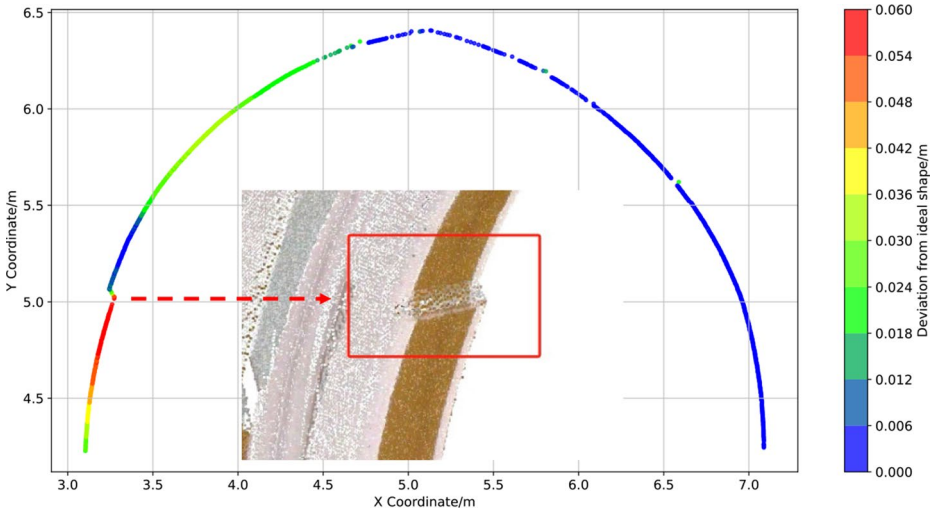

Fig. 8 Distortion evaluation in St. Ilias Orthodox Church

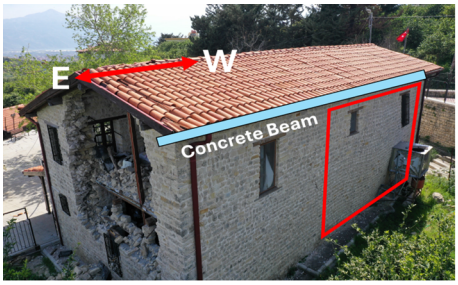

(a) Aerial photograph of the building.

(b) Photograph of bulging in N wall.

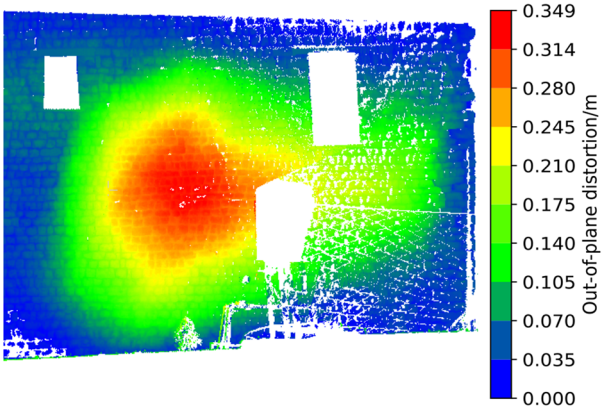

(c) N wall out-of-plane distortion from TLS point cloud comparison with vertical plane.

(d) Later photograph showing collapse of the bulging area in N wall

Fig. 9 Geometric distortion analysis of the Vakifli #2 building

as shown in Fig. 9. Maximum out-of-plane bulging of 34.9 cm can be observed from the contour plot. The two-way bending distortion pattern indicates the presence of a restraint at the top of the wall. The large magnitude of the bulging distortion indicates the notable plasticity of the modern restoration mortar used on the surface.

Inspired by these observations, recent field examination of this structure in 2024 has indicated the presence of a concrete beam running along the top of the longitudinal wall. A recent failure of the bulging area was also noted (Fig. 9b) (likely due to creep effects), which highlighted internal separation between wall leaves. Poor-quality straw and earth mortar were observed in the internal areas of the wall, which might have facilitated the separation between the wall leaves and the observed bulging behaviour.

4.1.3 St. George Sarilar Orthodox Church

St. George Sarilar Orthodox Church is thought to be dated from the 14th century and is located in the Altinozu district of Hatay. The earthquakes resulted in a major collapse of one of its two stone cross vaults (e.g. the east vault), as shown in Fig. 10a. The standing vault to the west is highlighted in the figure. This structure is on the 2024 Europa Nostra shortlist for the 7 Most Endangered buildings in Europe.

To understand how the west vault resisted the seismic loading while the adjacent and the geometrically similar east vault collapsed, a quantitative assessment of its geometric distortions was conducted using point cloud data. The distortion of the internal face of the southern wall supporting the west vault is shown in Fig. 10b, where the colours indicate the horizontal distance between a primitive vertical plane and the point cloud. Note that two orthogonal elevation views of the same wall is provided Fig. 10b. A large southward movement, measuring 30 cm at the top of the wall, is observed, indicating more than 5% lateral residual drift. Site observations demonstrated that the construction gaps between the modern reinforced concrete porch and the southern wall have closed due to these displacements, with the wall abutting on the porch. The porch appears to have arrested the lateral movements of the south wall supporting the vault, preventing collapse.

The accompanying distortions in the vault are challenging to analyse since the original non-circular geometry cannot be reliably estimated from the heavily distorted point clouds. Furthermore, drawings are not available for this church. However, assuming that the crowns of the vault quadrants were originally located at the same elevation, deviations between a horizontal plane (representing the undeformed height of the crown) and the point cloud can be evaluated, as illustrated in Fig. 10a. The horizontal plane is located at the height of the highest crown of the four quadrants. This distortion suggests a large depression at the centre of the vault exceeding 30 cm. Downward movement of the crown is consistent with the lateral movement of the east wall, which increased the span of the vault. These analyses demonstrate the utility of point clouds in unravelling distortion mechanisms, which are difficult to identify with the naked eye.

4.2 Crack measurement

Crack assessment is a key procedure in classifying damage levels, typically involving measurements of crack width, length, pattern, and distribution. These features are often analysed alongside other damage indicators, such as geometric distortions. In this section, we demon-

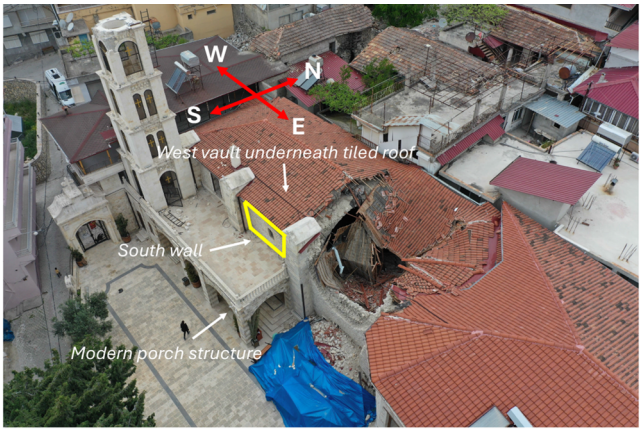

(a) An aerial photograph of the church.

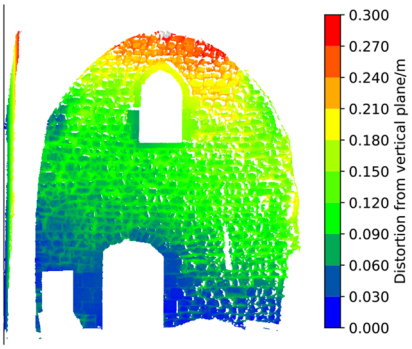

(b) Elevation views of the S wall out of plane distortions obtained from comparisons between TLS data and a vertical plane.

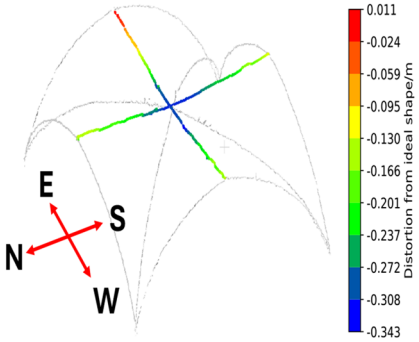

(c) Perspective views of the W vault out of plane distortions obtained from comparisons between TLS data and a horizontal plane.

Fig. 10 Distortion evaluation of St George Sarilar Orthodox Church

strate how point cloud data can offer a more effective alternative to traditional methods for measuring crack widths, especially when cracks are inaccessible.

4.2.1 St George Sarilar Orthodox Church

As an example, the standing west vault in St George Sarilar Orthodox Church exhibited smeared cracking in different parts of the vault (see Fig. 11a). In some locations, stone units had fallen off and large gaps had appeared in the vault soffit. Measurements of some cleaner cracks (with widths in the order of centimetres) were acquired from point-to-point distances between crack edges. These measurements are illustrated in Fig. 11b. Where a worm's eye view of the vault is provided. To do this analysis, photogrammetry point clouds were used, since their realistic representation of colour helps identify crack edges (where there is a transition to darker colours). It should be noted that the manual pointwise measurement of

cracks is only suitable for cases where the size of the crack is notably larger than the measurement accuracy of the point cloud (Lague et al. 2013).

4.2.2 Agcabey mosque minaret

Agcabey mosque was originally constructed during the 15th century. The building is located in the Bahce district of Osmaniye. Although the prayer hall building was reconstructed during the 19th century, the minaret (see Fig. 12a) is thought to date from the original construction. The stone voussoirs of the minaret experienced large amounts of sliding during the earthquake, causing through thickness separations between the units.

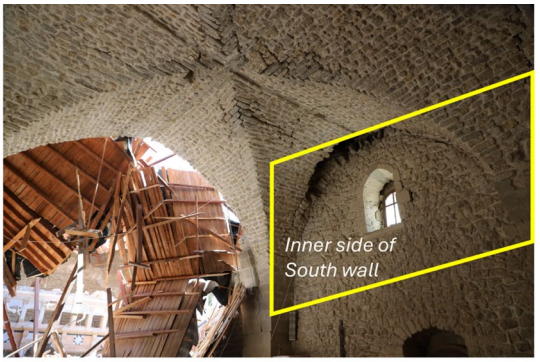

(a) Interior view.

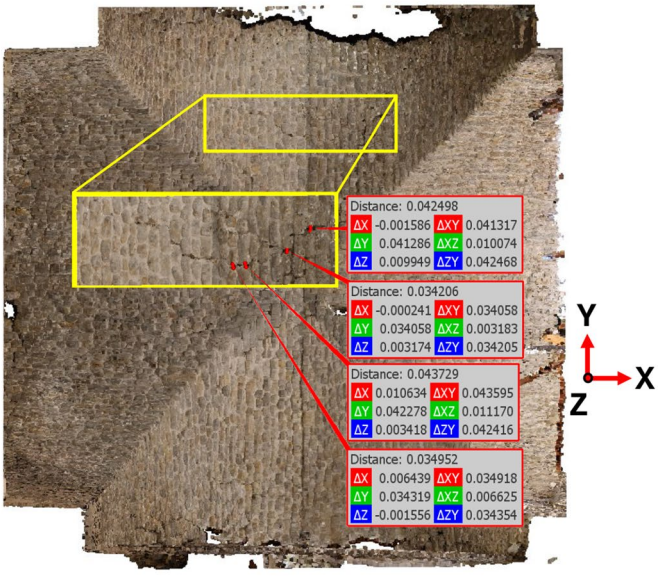

(b) Manual crack measurements from the photogrammetry point cloud of the St George Sarilar Orthodox Church west vault using point to point distances.

Fig. 11 West vault in St George Sarilar Orthodox Church

Drone photographs were used to generate point clouds since the minaret was otherwise inaccessible. The edges of the large shear crack are delineated clearly in the point cloud in Fig. 2b. To see the variation in crack openings, the crack edges were manually segmented and the closest distance between the edges was determined. Different from the procedure adopted earlier in Fig. 11b, the closest distance was evaluated from the distances between locally fitted planes on the crack edges to minimise the influence of measurement noise on the crack width measurements. The result is shown in Fig. 12b. Where crack widths up to 12 cm can be observed. The width first increases and then reduces with increasing height.

4.2.3 St. Ilias Church

The previous analyses involved some manual steps to conduct crack measurement which may introduce bias. In both cases, manual processing interventions were necessary due to the large surface roughness exhibited by the point clouds which causes occlusions and makes colour-based automatic segmentation of cracks difficult. Automatic analysis of cracks can be performed in smoother surfaces where drastic colour changes are isolated at the crack locations. This is the case for the apse of St. Ilias Church (see Fig. 13a) where the cracks appear darker than the surrounding masonry due to limited illumination of these emerging gaps. Automatic detection and measurement are performed using the photogrammetry point clouds as follows: 1) segmenting points identified as cracks on the basis of colour clustering, 2) labelling the edges of the cracks via connected component labelling, 3) identifying the crack faces by finding the convex hull of the segmented regions, and 4) computing the shortest distance between the crack faces (using local fitting to minimise distance measurement errors). It should be noted that the last step of this operation is identical to the analyses in Fig. 12b for the minaret of the Agcabey Mosque.

Figure 13b presents the final crack opening map of the St Ilyas apse, where a maximum crack width of 10 cm can be observed. Only the top part of this crack was analysed, the crack continues (with smaller widths) at lower elevations.

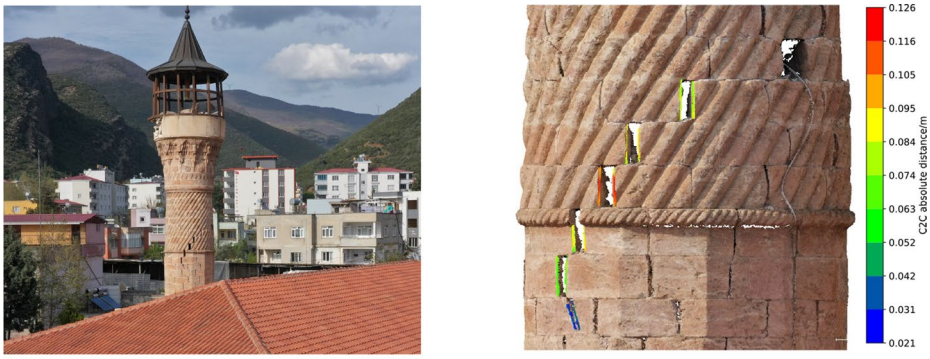

(a) Aerial photograph. (b) Crack measurements.

Fig. 12 Semi-automated crack measurements from the photogrammetry point cloud of the minaret of the Agcabey mosque using plane to plane distances

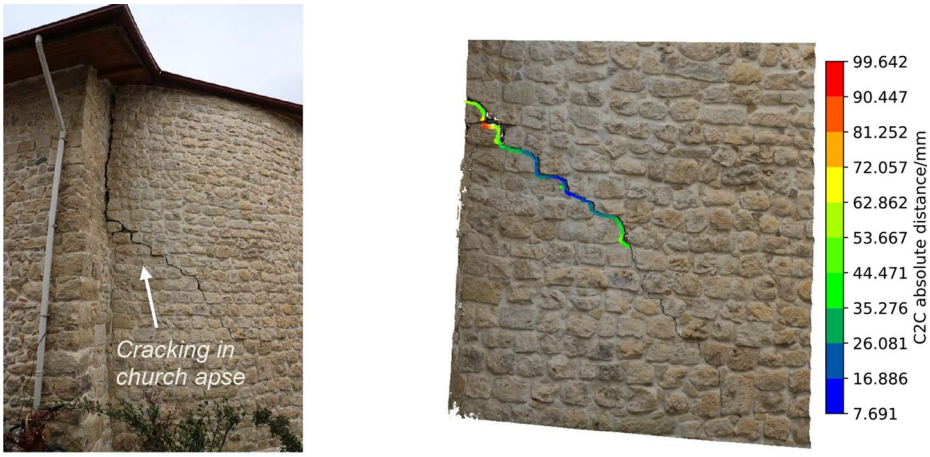

(a) Image data. (b) Crack measurements.

Fig. 13 Fully automated crack measurements from the photogrammetry point cloud of the apse of St Ilias church

4.2.4 Conclusion

In this section, crack assessment is carried out using various techniques applied to point cloud data obtained through scanning and photogrammetry. This approach enables the measurement of cracks that may be inaccessible to on-site inspectors. Unlike image-based methods, point clouds do not require scale calibration, allowing for direct measurement of crack lengths and widths. Additionally, they offer a clearer understanding of the spatial distribution of cracks across the structure.

5 Numerical simulations

This section presents a case study on how post-earthquake laser scanning data from St Nicholas church was used to generate and evaluate numerical models.

St. Nicholas is a late 19th century church from the Iskenderun district of Hatay province. It suffered significant damage during the earthquake, due to the insufficiency of its load-bearing walls to resist seismic demands, according to the simple index calculations in Bozyigit et al. (2024). The smeared cracking experienced in the south wall of the church is shown with a photograph in Fig. 14a. Corner failure debris can also be seen in the photograph.

To quantify the residual geometric distortions, out-of-plane distortions of the south façade point cloud (see Fig. 14a) from a vertical plane were calculated. Figure 14b highlights up to 4 cm northward (towards the church nave) displacement in the central part of the wall, and southward 2 cm displacement near the corners. The drastic change of colour in the region between the openings (highlighted with a red bounding box) indicates sliding cracks, which is in agreement with the observation of small crack openings in Fig. 14a. It should be noted that without scanning data, the magnitude and direction of the cracks would not have been apparent from visual observations alone. The data indicates that a rocking response

mechanism may have initiated in this part of the wall, where sliding may have occurred at the rocking interface.

The points within the target region are further processed to quantify sliding, by following the procedure outlined herein: 1) The 3D points within the region are mapped to a grey-scale image, with out-of-plane deviations representing the intensity of pixels. This is done by first creating a mesh for the pixels and using linear interpolation of the deviation values. 2) The crack locations are identified with Watershed segmentation (Vincent and Soille 1991) by enforcing the upper part to be the background. 3) Misclassified pixels are manually filtered. Figure 14c shows the cleaned results. 4) Crack quantification is done by evaluating the mean difference between the deviations above and below the identified crack edge. The final contour map is shown in Fig. 14d, where a maximum sliding of 11.8 mm can be observed.

Finite element (FE) models are created to simulate the earthquake response, using the software Abaqus (Dassault Systemes Simulia Corp 2017). Thin shell elements (with ID: S4R) are used to model the building and apse walls. Masonry is represented as a homogenous continuum in the models. Recent drawings of the structure were available and were used to form the geometry. Figure 15a shows the mesh used for the analyses, where the characteristic mesh size is 200 mm.

Construction drawings provided limited information regarding roof structures. Therefore, point clouds and drone photography data were examined to establish that the roof structure is composed of thin timber vaults, overlain by wood planks. From the photographs, it was evident that the timber roof could not provide noteworthy lateral stiffness. Estimates of roof weight also indicated negligible dead loads. Hence, the roof was not considered in the finite element model. The model is assumed to be fixed at the base.

A limited number of non-destructive tests (10 Schmidt Hammer and Ultrasonic Pulse Velocity tests on stones and 2 Penetrometer tests on mortars) were conducted during the fieldwork to estimate the compressive strength of the stones f_s and mortar f_m. Due to the small number of measurements, these results were not reported in Bozyigit et al. (2024), but data collection followed the techniques specified therein. An average compressive strength of 8.9 MPa was obtained for the stones, with a coefficient of variation of 20%. An average compressive strength of 1.4 MPa was obtained for the mortar. The average compressive strength of masonry f_c was estimated from the unit and mortar compressive strength following Eurocode EN 1996-1-2:2024 equations as 3.45 MPa, assuming a coefficient of variation of 20%.

The constitutive model used for the numerical simulations is the Concrete Damage Plasticity Model (CDP) (Lee and Fenves 1998). Since compression failures were not observed, simulations considered linear elastic behaviour in compression. A simple linear softening relationship was adopted in tension. The compressive strength estimations from the non-destructive data were used to estimate the material parameters, following the correlations provided by Illampas et al. (2020), TBER (2018) Lourenco (2009), and Kaushik et al. (2007). The critical tensile strength parameter was taken as 10% of either masonry or stone strength. The former value provides a reasonable estimate while the latter provides an upper bound estimate of this parameter. The ratio of ultimate strain to peak strain in tension was taken as 10. The adopted material properties are summarised in Table 6.

Other parameters required for the CDP model were obtained from Zizi et al. (2021); Jain et al. (2020a); Malcata et al. (2020); Milani et al. (2019). Table 7 presents the numerical values of the dilation angle, Ψ, the flow potential eccentricity, ε, the ratio of the second stress

(a) South façade.

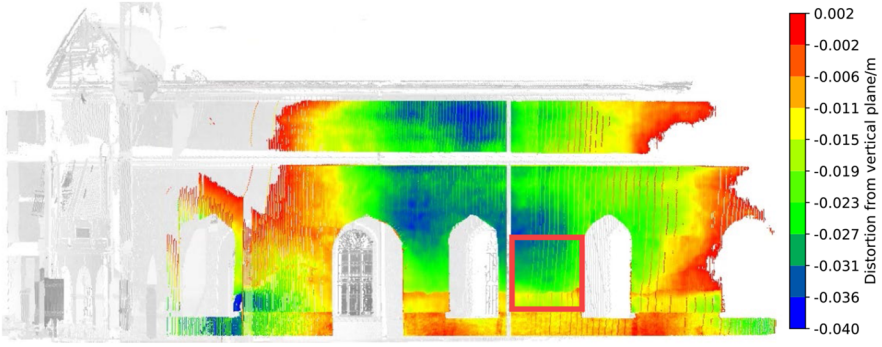

(b) Distortion of the south façade. Positive values indicate southward displacements.

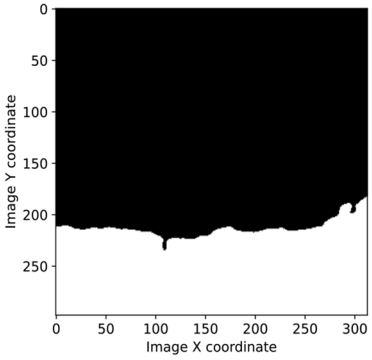

(c) Identification of sliding failure location.

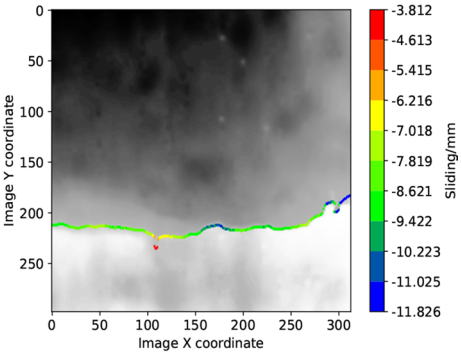

(d) Measurement of sliding magnitude.

Fig. 14 Distortion evaluation of Church of Saint Nicholas. The target region is highlighted by the red bounding box in (a)

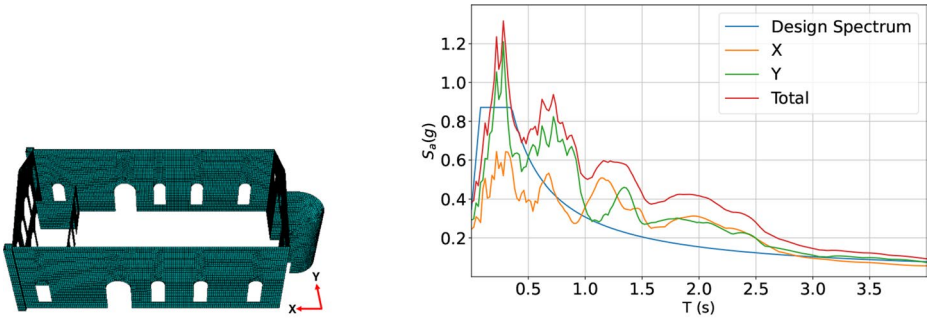

(a) FE model. (b) Earthquake spectrum used in simulations.

Fig. 15 Setup of FE simulations

Table 6 Material properties used in finite element simulations

	$f_c(MPa)$	$f_t(MPa)$	
Assessment method	$f_c = 0.69 f_s^{0.7} f_m^{0.3}$	$f_t = 0.1 f_c$ or $f_t = 0.1 f_s$	
Values	3.45	0.345 or 0.89	
	$E(MPa)$	$\rho(kg/m^3)$	$\varepsilon_u/\varepsilon_p(-)$
Assessment method	$E = 1000 f_c$	-	-
Values	3450	1600	10

Table 7 Additional parameters used in Abaqus

Ψ	ε	K_c	μ
10°	0.1	2/3	0

invariant on the tensile meridian to that on the compressive meridian, K_c, and the viscosity parameter governing the visco-plastic regularization, μ. The dilation angle (Ψ), defined as internal friction of the material, has been reported to vary between 10°–30° in the literature (Bagherzadeh Azar and Sari 2024; Upadhyaya et al. 2024; Dabiri et al. 2025; Nastri et al. 2025; Remus et al. 2025). In this study, a value of 10° is used, consistent with previous investigations on stone masonry by Dabiri et al. (2025); Yavartanoo et al. (2025); Kamath and Krishnamoorthy (2022); Jain et al. (2020b); der Pluijm et al. (2000). Rayleigh damping (Chopra and McKenna 2016) was adopted for the analyses.

Non-linear time history analyses were conducted using the acceleration data of the accelerometer closest to the church (4.2 km). This data is available in website of Disaster and Emergency Management Presidency (AFAD 2025) with the ID 3115. The acceleration time history was clipped to include only its effective duration, defined as the time interval where the normalised Arias intensity is in the range 5% to 95%. The ground conditions at the building and accelerometer sites are comparable, as indicated by similar average shear wave velocities in the upper 30 metres depth, $(V_s)_{30}$, recorded at both locations (TechReport 2023; AFAD 2025). The response spectra associated with the clipped earthquake record is shown in Fig. 15b. Explicit time stepping was used with a time step of 0.01 s.

Figure 16 shows the final state of the tensile damage variable output DAMAGET (the tensile damage indicator in Abaqus, varying from 0 to 1 with increasing severity) for the

two analyses with different tensile strength values. The proximity of this variable to its maximum value of 1 across a range of locations indicates significant and smeared damage accumulation. It can be observed that there is a strong correspondence between the locations where high values of DAMAGET are observed in Fig. 16 and visible crack locations on the south façade (see Fig. 14a). In particular, the location of horizontal cracks at the corners of door and window openings are notably similar. These observations appear to vindicate the modelling assumptions and highlight the insufficiency of transverse load bearing walls.

However, further comparisons between the residual out of plane displacements from the models in Fig. 17 to the equivalent laser scan measurements in Fig. 14 reveals some important differences. The horizontal residual displacements at the top of the central area of the south façade is 40 cm northwards according to laser scan data, whilst it is 50 cm and 178 cm northwards in the finite element simulations. It is apparent that the displacement predictions are sensitive to the choice of the tensile strength parameter.

The maximum displacements from the high tensile strength simulation and laser scans are similar but the pattern of displacements are notably different. Whilst an abrupt change

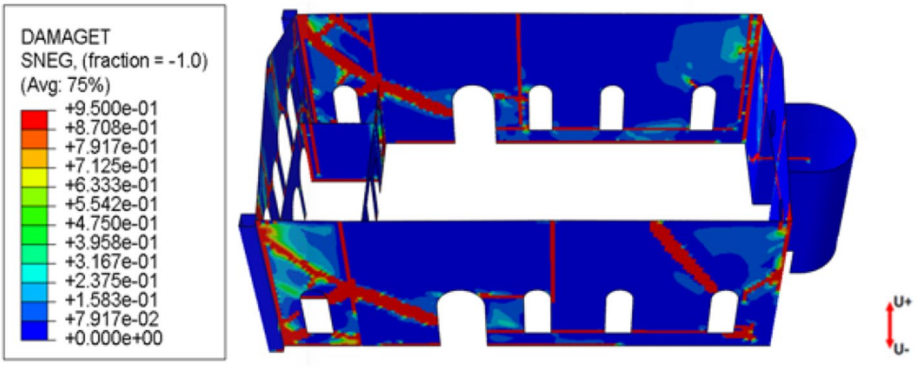

(a) $f_t = 0.345$ MPa.

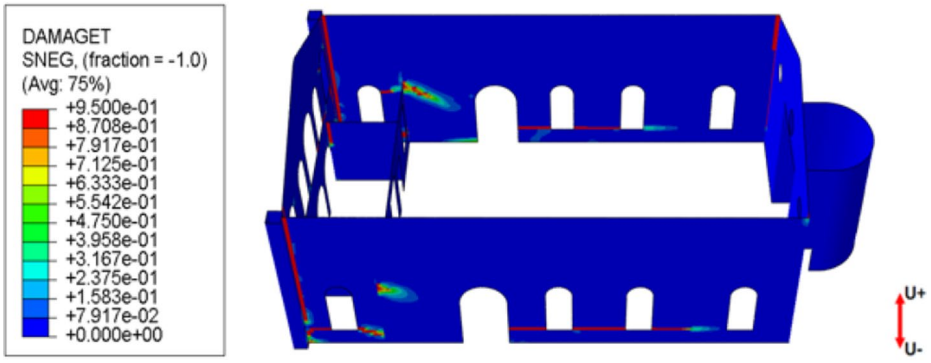

(b) $f_t = 0.9$ MPa.

Fig. 16 Damage map from FE simulations. Bottom face of the model is the south façade

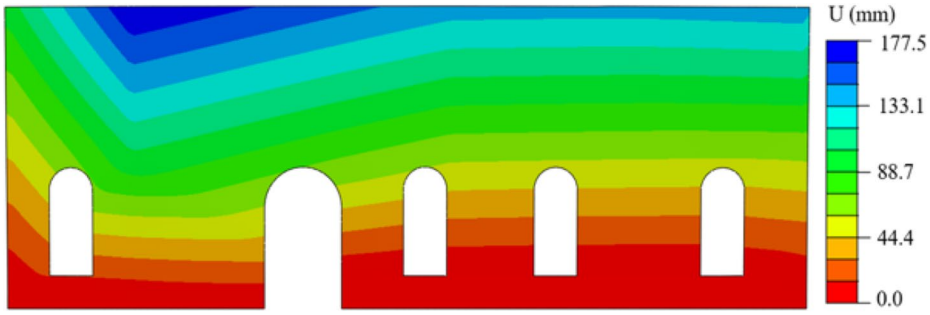

(a) $f_t = 0.345$ MPa.

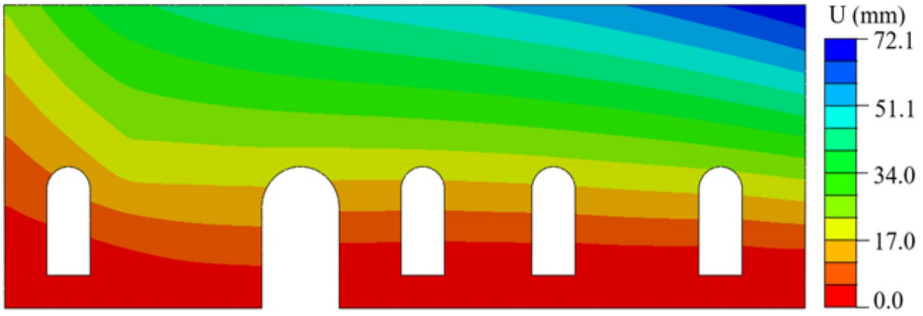

(b) $f_t = 0.9$ MPa.

Fig. 17 Residual displacement of the south façade

in laser scan data indicates that a sliding mechanism is partially responsible for the large residual displacements, simulations indicate a gradually increasing displacement pattern, due to the formation of rotational hinges around the bases of the windows. To address this difference with simulations, it would be necessary to adopt a micro-scale representation of masonry, where sliding can be explicitly simulated. It should also be noted that the simulation with the lower (but more realistic) tensile strength parameter significantly overestimates the residual displacements. This discrepancy may be due to the recognised limitations of continuum modelling techniques in simulating rigid body rocking motion.

It is important to recognise that tensile strength represents only one of numerous key parameters influencing the structural response; factors such as boundary conditions can also exert a substantial effect on the structural response. However, further improvement of the model was not judged necessary for the outcomes of this paper, the goal of which is to demonstrate how deeper insight can be obtained from point clouds to guide numerical model generation and evaluation. The results in this section demonstrate how the distortion data from laser scans provides valuable quantitative data which allows interrogating model accuracy beyond visible crack locations.

6 Conclusions

This paper explores the application of laser scanning and photogrammetry point clouds in post-earthquake reconnaissance. It emphasizes the additional insights provided by this alternative data source, particularly in enhancing forensic damage evaluations. Case studies involving several masonry structures damaged during the 2023 Turkey earthquake sequence are presented to demonstrate the findings.

First, derivation of critical geometric information from point clouds is discussed. The use of this data to generate simple indicators of structural capacity or to characterise complex aspects of geometry is highlighted. Then, a semi-automated method is developed for assessing the construction quality of masonry structures using point cloud data. This involved translating qualitative descriptors of masonry quality index from previous publications into new quantitative metrics and developing automated data analysis procedures for morphological analysis.

Beyond geometry and construction quality, structural damage is quantified using distortion evaluation and crack measurements from point clouds. Case studies highlight how such analysis may be used to identify deformation patterns that may not be visible to the naked eye. The quantitative distortion information provided a useful measure to assess numerical simulations, and highlighted key differences which may not have been observed otherwise. This highlights the potential of point cloud data to guide the development of improved models for forensic analysis.

However, many of the data processing tasks, particularly the segmentation of individual brick units, continue to demand significant manual effort. With the ongoing advancement of learning-based techniques in the field of point cloud processing, this limitation is expected to be mitigated in future research. Furthermore, the availability of point cloud data capturing the structure at various stages would enable more comprehensive displacement and crack assessments, as indicated in Liu et al. (2025).

Overall, this study shows that laser scanning and photogrammetry are efficient and readily-accessible techniques for forensic evaluations in post-earthquakes, which can improve upon traditional approaches. All data used in this research will be made publicly available to support further developments of these techniques.

Appendix A Additional tables

Table A1 List of surveyed structures

ID	Building Name	Province	District	Coordinates	Laser Scanning	Aerial Photos	Terrestrial Photos
C1	St Karasun Manuk Church	Hatay	Iskenderun	36.589470, 36.170399	√	√	√
C2	St Nicholas Orthodox Church	Hatay	Iskenderun	36.587394, 36.170450	√	√	√
C3	Latin Catholic Church	Hatay	Iskenderun	36.591034, 36.168236	√	√	√

Table A1 List of surveyed structures

ID	Building Name	Province	District	Coordinates	Laser Scanning	Aerial Photos	Terrestrial Photos
C4	Syriac Catholic Church	Hatay	Iskenderun	36.589645, 36.168987	√	√	√
C5	Batıayaz Church	Hatay	Samandağ	36.166678, 35.989150	√		√
C6	Virgin Mary Samandağ Orthodox Church	Hatay	Samandağ	36.101582, 36.259707	√		√
C7	St. Ilias Orthodox Church	Hatay	Samandağ	36.097664, 35.991638	√	√	√
C8	St George Sarılar Orthodox Church	Hatay	Antakya	36.120786, 36.253274	√	√	√
C9	Virgin Mary Tokaçlı Orthodox Church	Hatay	Altınözü	36.101582, 36.259707	√	√	√
C10	Sr George Iskenderun Orthodox Church	Hatay	Antakya	36.590412, 36.169708			√
M1	Habib-i Neccar Mosque	Hatay	Antakya	36.201650, 36.165590	√	√	√
M2	Sarimiye Mosque	Hatay	Antakya	36.199821, 36.163920	√		√
M3	Sheikh Ali Mosque	Hatay	Antakya	36.202496, 36.167433	√	√	√
M4	Kursunlu Han Mosque	Hatay	Antakya	36.202933, 36.163859			√
M5	Enverul Hamit Mosque	Osmaniye	Merkez	37.072526, 36.251681	√	√	√
M6	Agcabey Mosque	Osmaniye	Bahce	37.204566, 36.581948	√	√	√
M7	Ala Mosque	Osmaniye	Kadirli	37.372687, 36.101837	√		√
M8	Hamidiye Mosque	Osmaniye	Kadirli	37.372685, 36.098481	√		√
P1	Antakya Metropolitan Municipality Building	Hatay	Antakya	36.202633, 36.159859	√	√	√
P2	Mithatpasa School Annex Building	Hatay	Iskenderun	36.591112, 36.167914	√	√	√
P3	Yediocak Primary School	Osmaniye	Merkez	37.070550, 36.252231	√	√	√
P4	Antakya High School	Hatay	Antakya	36.204561, 36.155974			√
P5	Iskenderun High School	Hatay	Iskenderun	36.585550, 36.170974			√
P6	Workshop of Olive Museum	Hatay	Altınözü	36.101223, 36.260311	√		√
R1	Gali Mansion-I	Hatay	Antakya	36.202931, 36.169408	√	√	√

Table A1 List of surveyed structures

ID	Building Name	Province	District	Coordinates	Laser Scanning	Aerial Photos	Terrestrial Photos
R2	Gali Mansion-II	Hatay	Antakya	36.202933, 36.169408	√	√	√
R3	Hidirbey Gastronomy House	Hatay	Antakya	36.123093, 36.157022	√	√	√
R4	The English School	Hatay	Samandağ	36.085886, 35.989255	√	√	√
R5	Building #2 in Vakıflı	Hatay	Samandağ	36.115536, 35.974651	√	√	√

Acknowledgements The field work that supplied the data for this study was supported by EPSRC (grant nos. EP/P025641/1 and EP/V048082/1) and TUBITAK (2221-Fellowships for Visiting Scientists and Scientists on Sabbatical Leave Support Programme). The Earthquake Engineering Field Investigation Team (EEFIT) organized the first field mission. We thank FARO Technologies for providing software licenses that facilitated our research. Special thanks are due to Yixiong Jing, Zhengyou Zhang, and Anyu Shan for pre-processing the data, and to Kokcan Donmez for data collection.

Author contribution Yilong Yang: Conceptualization, Methodology, Software, Validation, Formal analysis, Data curation, Writing – original draft, Visualization. Elif Durgut and Medine Ispir: Methodology, Software, Validation, Formal analysis, Data curation, Writing – review & editing. Bora Pulatsu: Conceptualization, Resources, Writing – review & editing, Supervision. Sinan Acikgoz: Conceptualization, Methodology, Investigation, Resources, Data curation, Writing – review & editing, Supervision, Project administration, Funding acquisition.

Funding This work was supported by Engineering and Physical Sciences Research Council (EPSRC) (via grants EP/P025641/1 and EP/V048082/1) and TUBITAK (2221-Fellowships for Visiting Scientists and Scientists on Sabbatical Leave Support Programme).

Data availability The data used in this study is currently being curated to ensure its quality and usability. All registered point clouds will be made publicly available in an open data format prior to publication with a GitHub repository being prepared to host the data.

Declarations

Ethical approval The authors confirm that there are no ethical concernsassociated with this work.

Conflict of interest The authors declare no conflicts of interest.

References

AFAD (2025) Afad earthquake department. https://www.deprem.afad.gov.tr accessed: 2025-05-11

Aktaş YD, Ioannou I, Malcioglu FS, et al (2022) Hybrid reconnaissance mission to the. Front Built Environ 8:840192. https://doi.org/10.3389/fbuil.2022.840192
Aktaş YD, So E, Johnson C, et al (2024) The Türkiye Earthquake Sequence of February 2023: a longitudinal study report by EEFIT. Tech. rep., Earthquake Engineering Field Investigation Team (EEFIT), Institution of Structural Engineers (IStructE), https://doi.org/10.13140/RG.2.2.15906.40641
Awange J, Kiema J (2019) Fundamentals of photogrammetry. Environmental Geoinformatics. Environmental Science and Engineering Springer, Cham, https://doi.org/10.1007/978-3-030-03017-9_11
Bagherzadeh Azar A, Sari A (2024) Structural failure of masonry arch bridges subjected to seismic action. Civ Eng Infrastruct J https://doi.org/10.22059/ceij.2024.366834.1975, https://ceij.ut.ac.ir/article_96142.html
Barazzetti L, Banfi F, Brumana R, et al (2015) Cloud-to-bim-to-fem: structural simulation with accurate historic bim from laser scans. Simul Modell Pract Theory 57:71–87. https://doi.org/10.1016/j.simpat.2015.06.004, https://www.sciencedirect.com/science/article/pii/S1569190x15000994
Bianchi S, Hayez V, Lori G, et al (2024) Damage states of structural silicone glazed facades. In: Proceedings of the 18th World Conference on Earthquake Engineering (WCEE 2024)
Borri A, Corradi M, Castori G, et al (2015) A method for the analysis and classification of historic masonry. Bull Earthquake Eng 13:2647–2665. https://doi.org/10.1007/s10518-015-97314
Borri A, Corradi M, De Maria A (2020) The failure of masonry walls by disaggregation and the masonry quality index. Heritage 3(4):1162–1198. https://doi.org/10.3390/heritage3040065, https://www.mdpi.com/2571-9408/3/4/65
Bozyigit B, Ozdemir A, Donmez K, et al (2024)Damage to monumental masonry buildings in hatay and osmaniye following the 2023 turkey earthquake sequence: the role of wall geometry, construction quality, and material properties. Earthq Spectra 40(3):1870–1904 https://doi.org/10.1177/87552930241247031
Cardani G, Binda L (2015) Guidelines for the evaluation of the load-bearing masonry quality in built heritage, Springer International Publishing, Cham, 127–139. https://doi.org/10.1007/978-3-319-08533-3_11
Castellazzi G, Lo Presti N, D'Altri AM, et al (2022) Cloud2fem: a finite element mesh generator based on point clouds of existing/historical structures. SoftwareX 18:101099. https://doi.org/10.1016/j.softx.2022.101099, https://www.sciencedirect.com/science/article/pii/S235271102200067X
Chopra AK, McKenna F (2016) Modeling viscous damping in nonlinear response history analysis of buildings for earthquake excitation. Earthquake Eng Struct Dyn 45(2):193–211. https://doi.org/10.1002/eqe.2622, https://onlinelibrary.wiley.com/doi/abs/10.1002/eqe.2622
Conde B, Ramos LF, Oliveira DV, et al (2017) Structural assessment of masonry arch bridges by combination of non-destructive testing techniques and three-dimensional numerical modelling: application to vilanova bridge. Eng Struct 148:621–638. https://doi.org/10.1016/j.engstruct.2017.07.011, https://www.sciencedirect.com/science/article/pii/S0141029617306077
Contreras D, Wilkinson S, James P (2021) Earthquake reconnaissance data sources, a literature review. Earth 2(4):1006–1037. https://doi.org/10.3390/earth2040060, https://www.mdpi.com/2673-4834/2/4/60
Dabiri H, Marini R, Clementi J, et al (2025) Monitoring buildings performance using fea and ml based on the data acquired by insar; a case study of vittoriano building, rome. Structures 74:108643. https://doi.org/10.1016/j.istruc.2024.108643
Dassault Systemes Simulia Corp (2017) Abaqus Analysis User's Manual 6.13. Providence, RI, USA
der Pluijm RV, Rutten H, Ceelen M (2000) Shear behaviour of bed joints. In: Proceedings of the 6th North American Masonry Conference. Drexel University, Philadelphia, pp 125–136
Ergün Hatir M, İnce İ (2021) Lithology mapping of stone heritage via state-of-the-art computer vision. J Build Eng 34:101921. https://doi.org/10.1016/j.jobe.2020.101921, https://www.sciencedirect.com/science/article/pii/S2352710220335531
Hariri-Ardebili MA, Sattar S (2024) Data-Driven Insights Into Post-Earthquake Reconnaissance Findings: 2023 Türkiye Earthquake Sequence. Earthq Spectra 87552930241290485. https://doi.org/10.1177/87552930241290485
Ibrahim Y, Nagy B, Benedek C (2019) Cnn-based watershed marker extraction for brick segmentation in masonry walls. In: Karray F, Campilho A, Yu A (eds) Image Analysis and Recognition. Springer International Publishing, Cham, pp 332–344.
Illampas R, Ioannou I, Lourenço PB (2020) Seismic appraisal of heritage ruins: the case study of the st. mary of carmel church in cyprus. Eng Struct 224:111209. https://doi.org/10.1016/j.engstruct.2020.111209, https://www.sciencedirect.com/science/article/pii/S0141029620338104
Jain A, Acito M, Chesi C (2020a) Seismic sequence of 2016–17: linear and non-linear interpretation models for evolution of damage in san francesco church, amatrice. Eng Struct 211:110418. https://doi.org/10.1016/j.engstruct.2020.110418, https://www.sciencedirect.com/science/article/pii/S0141029619312507
Jain A, Acito M, Chesi C (2020b) Seismic sequence of 2016–17: linear and non-linear interpretation models for evolution of damage in san francesco church, amatrice. Eng Struct 211:110418. https://doi.org/10.1016/j.engstruct.2020.110418

Kamath K, Krishnamoorthy A (2022) Parametric study on laterite prism under uniaxial compression through numerical modeling. Materials Today: Proceedings 62:1564–1569. https://doi.org/10.1016/j.matpr.2022.02.361

Kassotakis N, Sarhosis V, Riveiro B, et al (2020) Three-dimensional discrete element modelling of rubble masonry structures from dense point clouds. Autom Constr 119:103365. https://doi.org/10.1016/j.autcon.2020.103365, https://www.sciencedirect.com/science/article/pii/S0926580520309456

Kaushik HB, Rai DC, Jain SK (2007) Stress-strain characteristics of clay brick masonry under uniaxial compression. J Mater Civil Eng 19(9):728–739

Laefer DF, Truong-Hong L, Carr H, et al (2014) Crack detection limits in unit based masonry with terrestrial laser scanning. NDT E Int 62:66–76. https://doi.org/10.1016/j.ndteint.2013.11.001, https://www.sciencedirect.com/science/article/pii/S0963869513001461

Lague D, Brodu N, Leroux J (2013) Accurate 3d comparison of complex topography with terrestrial laser scanner: application to the rangitikei canyon (n-z). ISPRS J Photogramm Remote Sens 82:10–26. https://doi.org/10.1016/j.isprsjprs.2013.04.009, https://www.sciencedirect.com/science/article/pii/S0924271613001184

Lee J, Fenves GL (1998) Plastic-damage model for cyclic loading of concrete structures. J Eng Mech 124(8):892–900. https://doi.org/10.1061/(ASCE)0733-9399(1998)124:8(892)

Liu Y, Burd HJ, Acikgoz S (2025) Point cloud-based crack detection and measurement in masonry buildings subjected to settlement induced by underground construction. Tunnelling Underground Space Technol 162:106600. https://doi.org/10.1016/j.tust.2025.106600, https://www.sciencedirect.com/science/article/pii/S088677982500238X

Lourenco P (2009) Recent advances in masonry modelling: micromodelling and homogenisation. Multiscale Modeling in Solid Mechanics: Computational Approaches. https://doi.org/10.1142/9781848163089_0006

Lourenço P, Oliveira D, Leite J, et al (2013) Simplified indexes for the seismic assessment of masonry buildings: international database and validation. Eng Fail Anal 34:585–605. https://doi.org/10.1016/j.engfailanal.2013.02.014, https://www.sciencedirect.com/science/article/pii/S1350630713000757

Lourenco P, Roque J (2006) Simplified indexes for the seismic vulnerability of ancient masonry buildings. Const Build Mater 20:200–208. https://doi.org/10.1016/j.conbuildmat.2005.08.027

Loverdos D, Sarhosis V (2022) Automatic image-based brick segmentation and crack detection of masonry walls using machine learning. Autom Constr 140:104389. https://doi.org/10.1016/j.autcon.2022.104389, https://www.sciencedirect.com/science/article/pii/S092658052200262X

Malcata M, Ponte M, Tiberti S, et al (2020) Failure analysis of a portuguese cultural heritage masterpiece: bonet building in sintra. Eng Fail Anal 115:104636. https://doi.org/10.1016/j.engfailanal.2020.104636, https://www.sciencedirect.com/science/article/pii/S1350630720305562

McCormac JC, Sarasua WA, Davis WJ (2012) Surveying, 6th edn edn. Wiley

Meli R (1998) Structural engineering of historical buildings. Fundación ICA

Milani G, Esquivel YW, Lourenço PB, et al (2013) Characterization of the response of quasi-periodic masonry: geometrical investigation, homogenization and application to the guimarães castle, portugal. Eng Struct 56:621–641. https://doi.org/10.1016/j.engstruct.2013.05.040, https://www.sciencedirect.com/science/article/pii/S014102961300271X

Milani G, Valente M, Fagone M, et al (2019) Advanced non-linear numerical modeling of masonry groin vaults of major historical importance: st john hospital case study in jerusalem. Eng Struct 194:458–476. https://doi.org/10.1016/j.engstruct.2019.05.021, https://www.sciencedirect.com/science/article/pii/S0141029618342019

Napolitano R, Hess M, Glisic B (2019) Integrating non-destructive testing, laser scanning, and numerical modeling for damage assessment: the room of the elements. Heritage 2(1):151–168. https://doi.org/10.3390/heritage2010012, https://www.mdpi.com/2571-9408/2/1/12

Nastri E, D'Apice A, Todisco P (2025) Earthquake-proofing history: seismic assessment of caserta vecchia medieval bell tower. Bull Earthquake Eng 23(2):833–857. https://doi.org/10.1007/s10518-024-01706-6

Pesci A, Teza G, Bonali E, et al (2013) A laser scanning-based method for fast estimation of seismic-induced building deformations. ISPRS J Photogramm Remote Sens 79:185–198. https://doi.org/10.1016/j.isprsjprs.2013.02.021, https://www.sciencedirect.com/science/article/pii/S0924271613000646

Remus A, Tezcan S, Sun J, et al (2025)Seismic failure assessment using energy outputs of finite element analysis: a strategy for complex heritage masonry structures modeled with concrete damaged plasticity material. Buildings 15 (3) 318 https://doi.org/10.3390/buildings15030318

Sacco GLS, Battini C, Calderini C (2024) A case study of preliminary damage detection of two heritage vaults through geometric deformation analysis on 3d point clouds. Structures 68:107175. https://doi.org/10.1016/j.istruc.2024.107175, https://www.sciencedirect.com/science/article/pii/S2352012424013274

Sacco GLS, Ferrero C, Battini C, et al (2023) Combined use of deformation and structural analysis for the structural damage assessment of heritage buildings: a case study in the liguria region (Italy). Eng Fail Anal 147:107154. https://doi.org/10.1016/j.engfailanal.2023.107154, https://www.sciencedirect.com/science/article/pii/S1350630723001085

Saito K, Spence RJS, Going C, et al (2004) Using high-resolution satellite images for post-earthquake building damage assessment: a study following the 26 january 2001 gujarat earthquake. Earthq Spectra 20(1):145–169. https://doi.org/10.1193/1.1650865

Stałowska P, Suchocki C, Rutkowska M (2022) Crack detection in building walls based on geometric and radiometric point cloud information. Autom Constr 134:104065. https://doi.org/10.1016/j.autcon.2021.104065, https://www.sciencedirect.com/science/article/pii/S0926580521005161

Sürmeli BS (2019) Rural settlements of hatay mount musa and proposals for conservation of the traditional houses. Master's thesis, Istanbul Technical University, Graduate School of Science, Department of Architecture, Division of Restoration

Szabó S, Funari MF, Lourenço PB (2024) A mason-inspired pattern generator for historic masonry structures using quality indexes. Eng Struct 304:117604. https://doi.org/10.1016/j.engstruct.2024.117604, https://www.sciencedirect.com/science/article/pii/S0141029624001664

TBER (2018) Türkiye Building Earthquake Regulation. Official Gazette, No. 30364 (in Turkish)

TechReport (2023) Geophysical studies for determination of soil properties in iskenderun and antakya: 06 february 2023 pazarcık, elbistan (kahramanmaras) and 20 february 2023 yayladağı (hatay) earthquakes. Tech. rep., Alsancak, İzmir, in Turkish

Tong X, Hong Z, Liu S, et al (2012) Building-damage detection using pre- and post-seismic high-resolution satellite stereo imagery: a case study of the may 2008 wenchuan earthquake. ISPRS J Photogramm Remote Sens 68:13–27. https://doi.org/10.1016/j.isprsjprs.2011.12.004, https://www.sciencedirect.com/science/article/pii/S0924271611001584

Truong-Hong L, Laefer D (2013) Validating computational models from laser scanning data for historic facades. J Test Eval. https://doi.org/10.1520/JTE20120243

Upadhyaya S, Maurya SK, Singhal V, et al (2024)Nonlinear static and dynamic response of a random rubble stone masonry building with horizontal seismic bands. J Perform Constr Facil 38(5):04024038 https://doi.org/10.1061/(ASCE)CF.1943-5509.0001912

Valero E, Bosché F, Forster A (2018) Automatic segmentation of 3d point clouds of rubble masonry walls, and its application to building surveying, repair and maintenance. Autom Constr 96:29–39. https://doi.org/10.1016/j.autcon.2018.08.018, https://www.sciencedirect.com/science/article/pii/S0926580517309895

Vincent L, Soille P (1991) Watersheds in digital spaces: an efficient algorithm based on immersion simulations. IEEE Trans Pattern Anal Mach Intell 13(6):583–598

Whitworth MRZ, Giardina G, Penney C, et al (2022) Lessons for remote postearthquake reconnaissance from the 14 august 2021 haiti earthquake. Front Built Environ 8:873212. https://doi.org/10.3389/fbuil.2022.873212

Wu C, Yuan Y, Tang Y, et al (2022) Application of terrestrial laser scanning (tls) in the architecture, engineering and construction (aec) industry. Sensors 22(1) https://doi.org/10.3390/s22010265, https://www.mdpi.com/1424-8220/22/1/265

Yavartanoo F, Kim CS, Bolhassani D, et al (2025)Macro-modeling of cfrp strengthening in u-shaped masonry walls under combined vertical and out-of-plane loads. Eng Fail Anal 109664 https://doi.org/10.1016/j.engfailanal.2024.109664

Ye C, Acikgoz S, Pendrigh S, et al (2018) Mapping deformations and inferring movements of masonry arch bridges using point cloud data. Eng Struct 173:530–545. https://doi.org/10.1016/j.engstruct.2018.06.094, https://www.sciencedirect.com/science/article/pii/S0141029617338439

Zizi M, Corlito V, Lourenco P, et al (2021) Seismic vulnerability of masonry churches in abruzzi region, Italy. Structures 32:662–680. https://doi.org/10.1016/j.istruc.2021.03.013